

# 3D Simulation of an Integrated Wavelength Converter

Joachim Piprek,<sup>1</sup> Nicolas Trenado, John Hutchinson,<sup>a</sup> Jeffrey Hennes, and Larry A. Coldren  
Electrical and Computer Engineering Department,  
University of California, Santa Barbara, CA 93106  
<sup>a</sup> also with Intel Corporation, Portland, OR

## ABSTRACT

In this paper, we present three-dimensional (3D) simulation results for an integrated wavelength converter which monolithically combines a pre-amplifying receiver with a post-amplified sampled-grating distributed Bragg reflector tunable laser diode. The self-consistent physical model used in the simulation takes into account gain and absorption in the quantum wells, carrier drift and diffusion, and optical wave-guiding. In order to validate and calibrate the model, we compare the results to available experimental data. Microscopic physical processes inside the converter components are revealed and analyzed, such as receiver saturation effects.

**Keywords:** Optoelectronic integrated circuits, OEIC, wavelength converter, numerical simulation

## 1. INTRODUCTION

Our wavelength converter electrically couples an optical receiver for any input wavelength of the C band, e.g.,  $\lambda_{in} = 1530$  nm, with an optical transmitter for any other output wavelength of the C band, e.g.,  $\lambda_{out} = 1550$  nm (Fig. 1). The receiver integrates signal pre-amplification by a 500  $\mu\text{m}$  long semiconductor optical amplifier (SOA) and signal detection by a 50  $\mu\text{m}$  long waveguide photodiode (WPD). The optical signal is converted into an electrical signal that directly modulates a sampled-grating distributed-Bragg-reflector (SGDBR) laser diode which is integrated with a semiconductor optical amplifier (SOA) for signal enhancement.<sup>1</sup> The SGDBR laser can be tuned to emit at any wavelength of the C band.

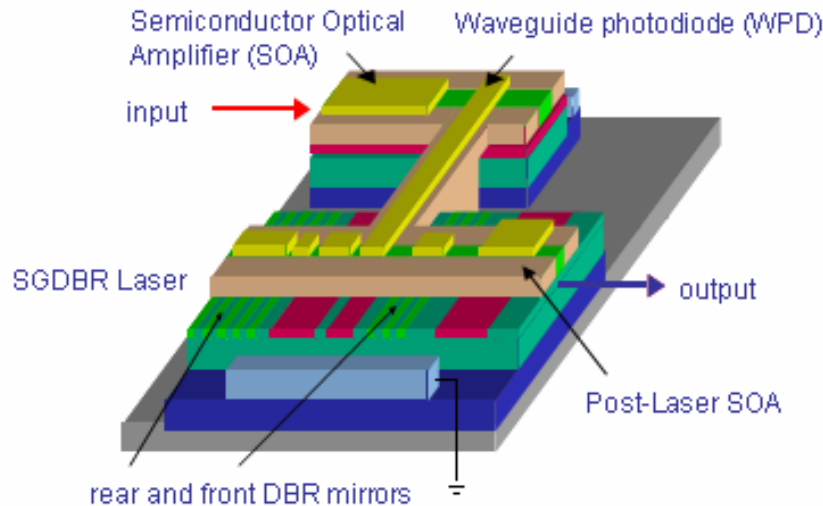


Fig. 1: Schematic view of the InP-based integrated wavelength converter.

<sup>1</sup> Corresponding author, e-mail: piprek@ieee.org

The structure of the different components is very similar as all are based on the same epitaxial growth (Tab. 1). An offset multi-quantum-well (MQW) active region is grown on top of the waveguide region. A ridge waveguide structure is etched through the MQW region. Passive device sections are formed by etching off the MQWs completely.

Layer	Material	Thickness nm	Doping $10^{18} \text{ cm}^{-3}$	Refractive index
p-contact	InGaAs	100	30 (p)	3.72
upper cladding	InP	1600	1 (p)	3.167
upper cladding	InP	200	0.3 (p)	3.167
doping setback	InP	50	-	3.167
quantum barrier (8x)	$\text{In}_{0.735}\text{Ga}_{0.265}\text{As}_{0.513}\text{P}_{0.487}$	8	-	3.396
quantum well (7x)	$\text{In}_{0.735}\text{Ga}_{0.265}\text{As}_{0.845}\text{P}_{0.155}$	6.5	-	3.616
etch stop	InP	10	-	3.167
waveguide	$\text{In}_{0.612}\text{Ga}_{0.338}\text{As}_{0.728}\text{P}_{0.272}$	350	0.1 (n)	3.455
lower cladding	InP	1400	1 (n)	3.167
etch stop / n-contact	InGaAs	100	1 (n)	3.72
Buffer	InP	1000	-	3.167

Tab. 1 Epitaxial layer sequence of the devices simulated.

The self-consistent numerical simulation<sup>2</sup> includes band-structure and gain calculations for the strained quantum wells, carrier transport, optical waveguiding, and Bragg reflection. Field effects on MQW gain and absorption (quantum confined Stark effect) are considered as well as free-carrier and intervalence band absorption. InGaAsP material parameters are adjusted based on recent publications.<sup>3</sup>

The next section discusses 2D simulation results and general device physics. The following section addresses the specifics of each device based on 3D simulation. Section 4 compares simulation results to available receiver measurements and discusses parameter calibration issues.

## 2. TWO-DIMENSIONAL SIMULATION

### 2.1 Optical Waveguiding

The software solves the scalar Helmholtz equation in two dimensions to obtain the intensity of the fundamental mode  $W_0(x,y)$ . The vertical profile  $W_0(0,y)$  is plotted in Fig. 2 together with the refractive index profile. The unsymmetrical index profile results in an optical confinement factor for the quantum wells of  $\Gamma=0.06$ . The 2D mode profile is given in Fig. 3. It is well confined by the p-InP ridge. In agreement with experimental results, fundamental mode operation is assumed here. Near  $1.55\mu\text{m}$  wavelength, optical losses are mainly caused by intervalence band absorption (IVBA). The IVBA coefficient is considered proportional to the local hole density, i.e., it is only relevant within the quantum wells and within p-doped regions. The total local absorption coefficient is calculated as

$$\alpha(x,y) = \alpha_b + k_n n + k_p p \quad (1)$$

with the background loss  $\alpha_b$ , the electron density  $n$  and the hole density  $p$ . The hole coefficient  $k_p = 25 \times 10^{-18} \text{ cm}^2$ , the electron coefficient  $k_n = 1 \times 10^{-18} \text{ cm}^2$ , and the background value  $\alpha_b = 10 \text{ cm}^{-1}$  are employed in our calculations.

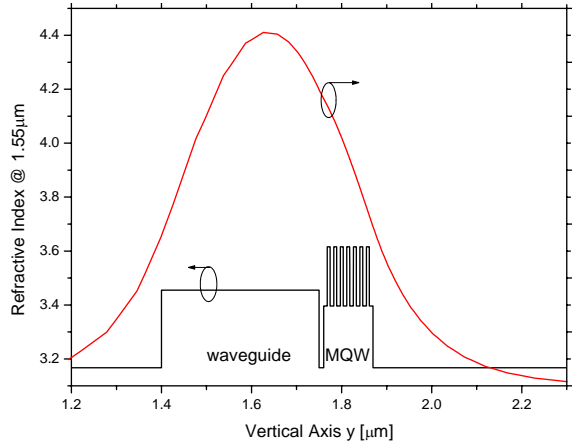


Fig. 2: Vertical profile of refractive index and optical intensity of the fundamental mode.

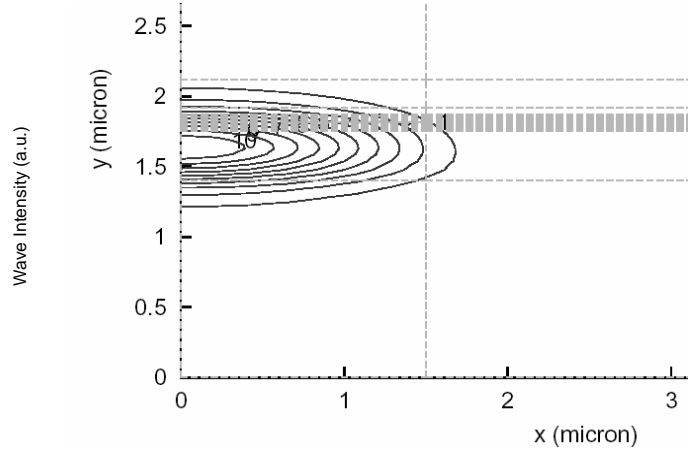


Fig. 3: 2D intensity profile of the fundamental waveguide mode for half the device ( $y$  – symmetry plane, ridge width = 3 μm).

## 2.2 Multi-Quantum Well Active Region

The energy band diagram of the multi-quantum well active region is plotted in Fig. 4. The etch stop layer is needed for longitudinal integration of different devices, however, it constitutes a barrier for electron injection into the MQW which requires thermionic emission of electrons from the waveguide layer. The common conduction band edge offset ratio  $\Delta E_c / \Delta E_g = 0.4$  is employed at all interfaces ( $E_c$  – conduction band edge,  $E_g$  - band gap). On the other hand, the etch stop layer also generates a barrier in the valence band, which helps to prevent holes from escaping the MQW.

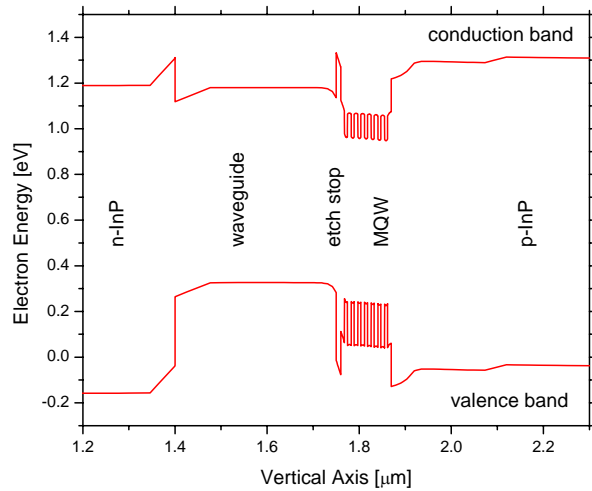


Fig. 4 Energy band diagram of the active region.

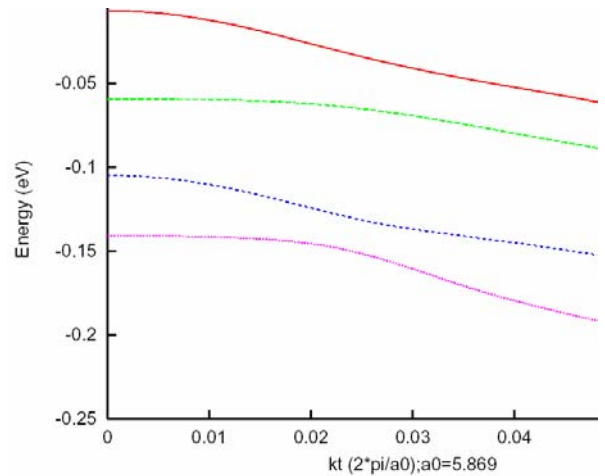


Fig. 5: Energy vs. transversal wavenumber for the quantum well valence subbands (from top: HH1, HH2, LH1, HH3).

For the quantum wells, compressive strain of 0.88% is calculated. The tensile strain in the barrier is -0.2%. The conduction bands are assumed parabolic with an in-plane effective mass of 0.0447. The non-parabolic valence bands are calculated using the popular  $4 \times 4$   $\mathbf{kp}$  method including valence band mixing (Fig. 5). Three heavy hole (HH) levels and one light hole (LH) level are found. The relevant top level has an effective HH mass of 0.3 at the  $\Gamma$  point.

### 2.3 Carrier Transport

The drift and diffusion of electrons and holes is calculated by solving the semiconductor transport equations.<sup>3</sup> For forward bias operation (95 mA) of amplifier or laser, Fig. 6 gives the vertical carrier density profile in the center of the device. The average quantum well carrier density is about  $2 \times 10^{18} \text{ cm}^{-3}$ . The lateral carrier density profile reveals relatively strong lateral carrier diffusion away from the waveguide ridge. The corresponding lateral profiles of the recombination rates are plotted in Fig. 7. Stimulated recombination is restricted to the fundamental optical mode profile (cf. Fig. 3). The strongest carrier loss is caused by the Auger recombination rate

$$R_{\text{Aug}} = n p (C_n n + C_p p) \quad (2)$$

with the preliminary Auger parameters  $C_n=0$  and  $C_p= 8 \times 10^{-29} \text{ cm}^6/\text{s}$ . Those parameters can later be adjusted to fit experimental characteristics. Spontaneous emission is calculated by integrating the spontaneous emission rate, it is proportional to the square of the carrier density. Shockley-Read-Hall (SRH) recombination at crystal defects and interfaces is inversely proportional to the SRH lifetime of the carriers. We here assume a uniform SRH lifetime of 20 ns for electrons and holes throughout the device. This value is longer than the total (measured) lifetime which includes all recombination mechanisms.

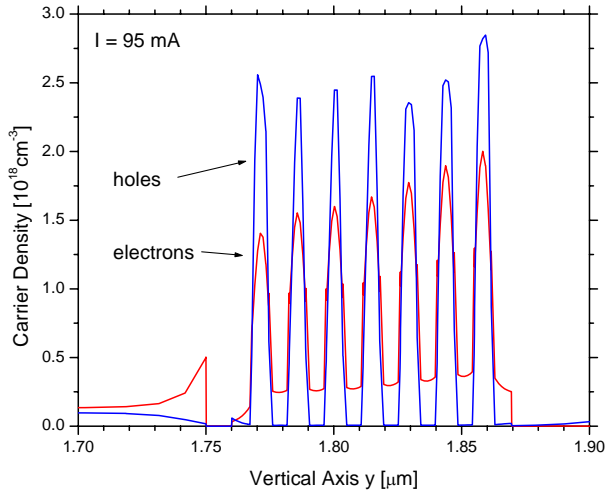


Fig. 6: Vertical carrier density profile in the center of the device.

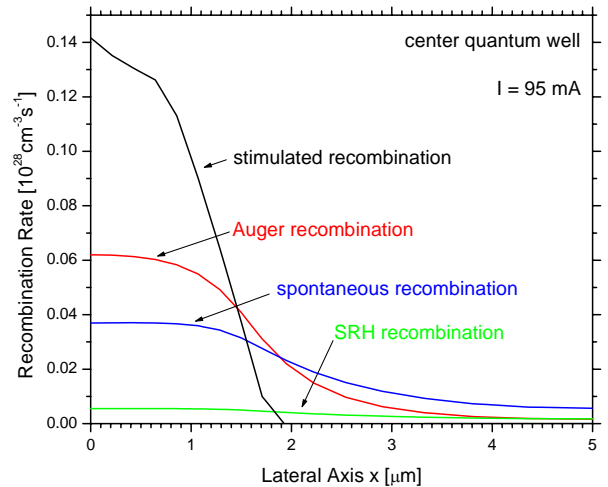


Fig. 7: Lateral profile of the quantum well recombination rates.

### 2.4 Quantum Well Gain and Absorption

Calculated gain spectra are shown in Fig. 8 under flat-band condition (zero field) using a free carrier model including Lorentz broadening with 0.1 ps intraband relaxation time. The gain peak wavelength blue-shifts slightly due to band filling, however, it is close to the target wavelength of 1550 nm. Figure 9 plots calculated quantum well absorption spectra for different reverse bias conditions of the photodetector. Higher reverse bias gives a stronger internal field which moves the absorption edge towards longer wavelength (quantum confined Stark effect). At the same time, the maximum possible absorption is reduced. At 2V reverse bias, our quantum well shows an absorption edge near 1610 nm. It absorbs light almost uniformly from 1500nm to 1600nm wavelength.

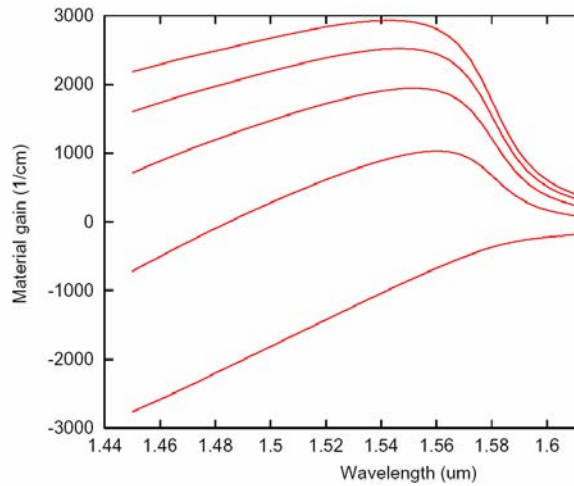


Fig. 8: Flat-band quantum well gain spectra for different carrier densities (from bottom: 1, 2, 3, 4, and  $5 \times 10^{18} \text{cm}^{-3}$ ).

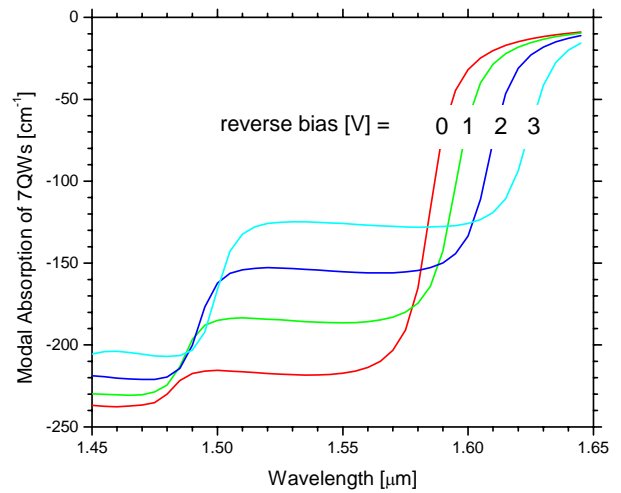


Fig. 9: Quantum well absorption spectrum at different bias.

### 3. THREE-DIMENSIONAL SIMULATION

#### 3.1 Waveguide Photodetector

Figure 10 shows a 3D plot of the optical intensity calculated for the fundamental mode with 0.01 mW input power. The optical power decays exponentially in travel direction ( $z$ ) and it is almost completely absorbed at the other end.

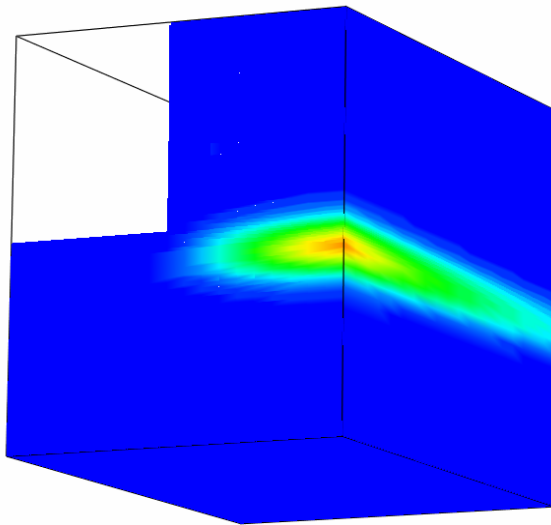


Fig. 10: Fundamental optical mode intensity for half the photodetector.

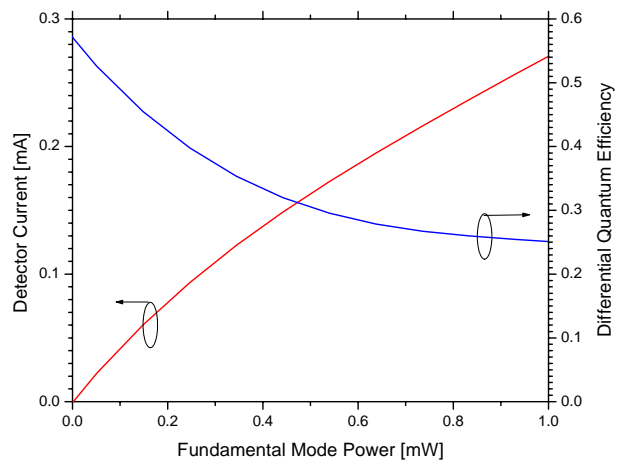


Fig. 11: Photocurrent and quantum efficiency vs. input power.

Photocurrent and quantum efficiency are given in Fig. 11. The calculation considers a front facet reflectance of  $R=0.29$ , which reduces the maximum possible quantum efficiency to 71%. At low input power, the calculated quantum efficiency is 58%, due to the incomplete absorption of the lightwave. With higher input power, the efficiency decays and it is only 25% at 1 mW. The decay in efficiency is reflected by the non-linear current-power characteristic in Fig.

11. The non-linear response of the photodetector is mainly attributed to the reduction of the quantum well absorption with increasing carrier density. The photon density is highest at the input facet. With increasing power, it generates an increasing number of electron-hole pairs in the quantum wells (QWs). The average QW carrier density is shown in Fig. 12 for different input power. Due to band filling, higher carrier density leads to lower absorption (Fig. 13) which affects the decay of the optical power along the waveguide (Fig. 14). With higher input power, the detection is less efficient, i.e., a larger part of the input power remains undetected. While the intensity decays by a factor of about 14 for low input power, it only decays by a factor of 5 for 1 mW input power in Fig. 14. This mechanism is the main reason for the non-linear photocurrent response shown in Fig. 11. The photocurrent is non-uniform in longitudinal direction (Fig. 15).

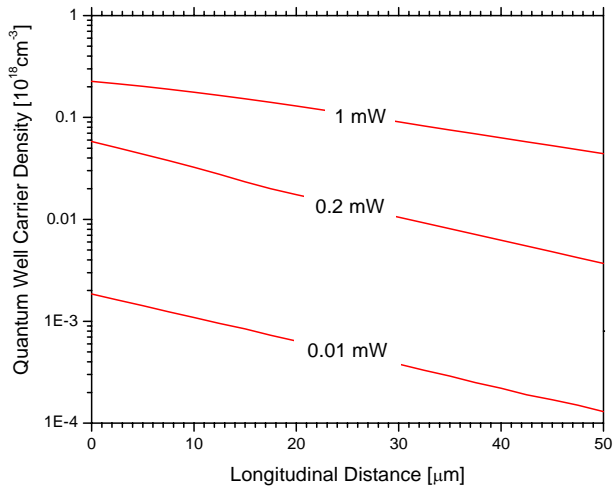


Fig. 12: Longitudinal profile of the quantum well carrier density at different input power.

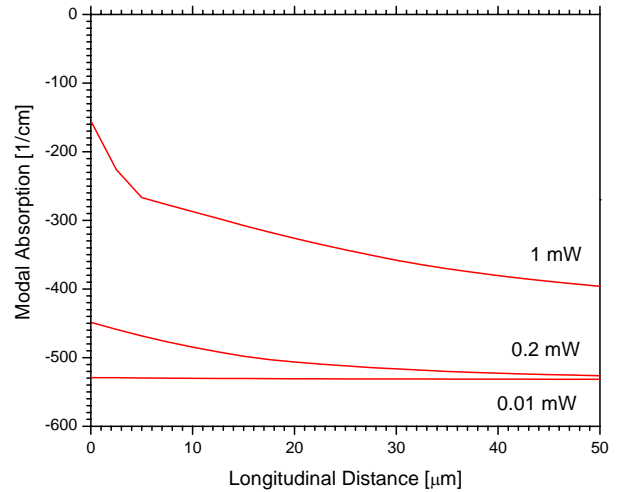


Fig. 13: Longitudinal profile of the modal absorption at different input power (1550 nm).

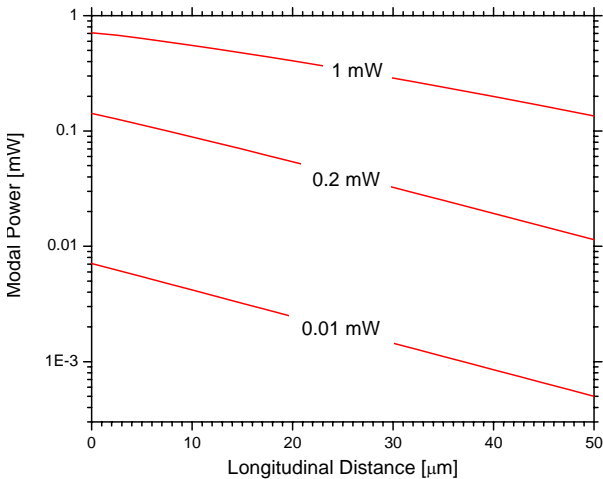


Fig. 14: Longitudinal decay of the modal power at different input power.

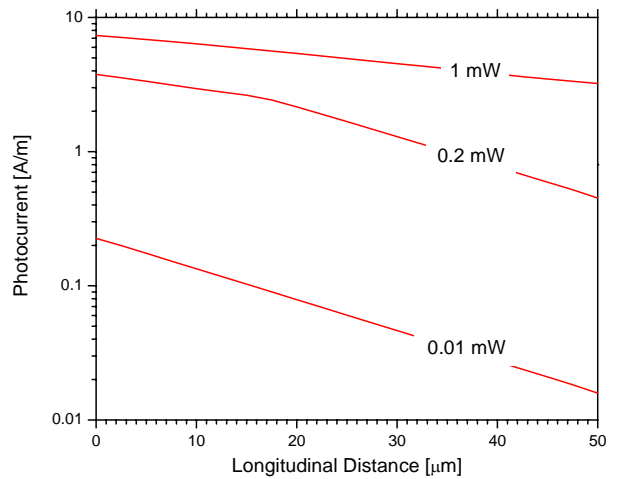


Fig. 15: Non-uniform distribution of the photocurrent at different input power.

However, it needs to be mentioned that PICS3D simulations are not truly 3D since carriers cannot move in longitudinal  $z$  direction. The device is rather sliced up into many 2D sections ( $x,y$ ) within which the device equations are solved self-consistently. The only difference between all the 2D sections is the photon density  $S(z)$  which varies in longitudinal

direction (Fig. 10). Thus, the quantum well carrier density  $N(x,y)$  varies among the 2D sections. Iteratively, a balance between  $S(z)$  and  $N(x,y)$  is achieved by the software which can be called quasi-3D solution.

### 3.2 Integrated Receiver

The optical gain of the MQW active region depends on the applied bias: if it is positive, the gain is positive and the region is an amplifying region, if the bias is negative, the gain is negative and the region is an absorbing region. The energy bands of the SOA region are plotted in Figure 16. The bands are flat due to presence of the doping region and the fact that a forward bias is applied to the SOA. In this case, the overlap between electron and hole wave function is optimum and the modal gain is positive (cf. Fig. 8). The energy bands of the WPD region are shown in Figure 17. A reverse bias is applied so that the bands are not flat and the absorption is dominant (cf. Fig. 9). The modal gain is positive for the SOA region and negative for the WPD region (Fig. 18). Accordingly, the wave intensity in Fig. 19 is increasing within the SOA region and decreasing within the WPD region.

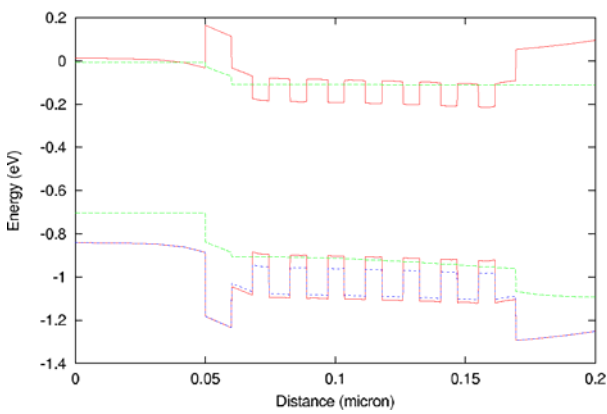


Fig. 16: Conduction (upper) and valence (lower) bands in the SOA region along the vertical y direction (dashed: quasi-Fermi levels)

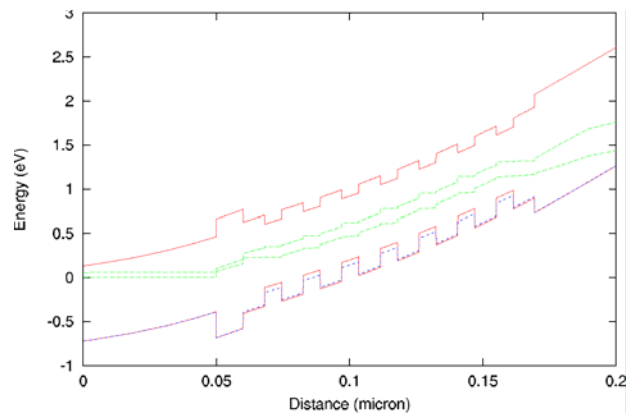


Fig. 17: Conduction (upper) and valence (lower) bands in the WPD region along the vertical y direction (dashed: quasi-Fermi levels)

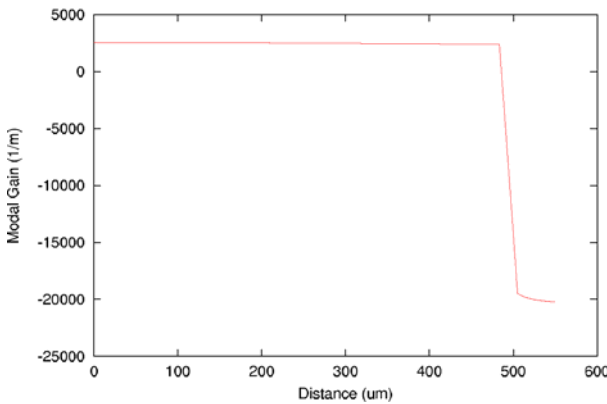


Fig. 18: Receiver modal gain along the longitudinal propagation direction z.

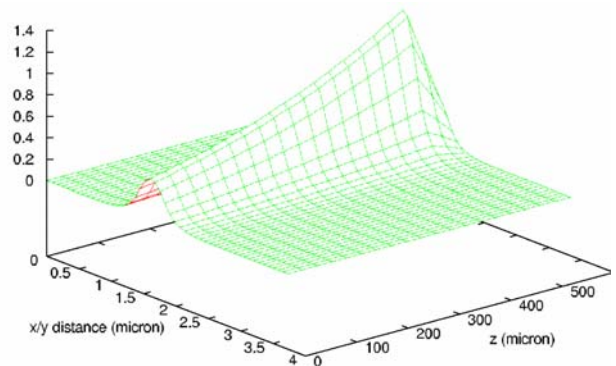


Fig. 19: Wave intensity surface plot (a.u.) within the vertical symmetry plane of the receiver ( $x=0$ ).

### 3.3 Integrated Transmitter

Simulation of the sampled-grating DBR laser diode<sup>4</sup> is the most challenging part of this project. The laser includes five longitudinal sections (Tab. 2). Optical gain is provided in the active section of the laser as well as in the amplifier. For this example simulation, both mirrors are tuned to exhibit reflectivity peaks at 1550 nm (Fig. 20). Laser emission is therefore at the same wavelength (Fig. 21). A 3D plot of the calculated wave intensity is shown in Fig. 22. In this case, the laser is biased well above threshold (25 mA). The amplifier current of 20 mA gives additional photon multiplication, resulting in a strong enhancement of the optical intensity towards the right facet of the emitter. The same situation is shown in Fig. 23 as longitudinal intensity profile, comparing two different amplifier currents. Within the SGDBR sections, each grating burst reflects part of the wave and gives a stepwise change in wave intensity. At low amplifier current (5 mA), the SOA region exhibits net optical loss and the optical intensity decays as the light approaches the right facet. SOA transparency is obtained at 16.5 mA. At higher SOA current net amplification is achieved.

The corresponding light-current (LI) characteristic is given in Fig. 24. Lasing threshold is calculated at about 14 mA. At first, the amplifier current is kept constant at 5 mA and the laser current is ramped up to 25 mA. The slope of the LI curve is 0.043 W/A which corresponds to a differential quantum efficiency of only 5% for the right facet, due to the photon losses in the amplifier. Second, the SOA current is ramped up to 20 mA keeping the laser current constant at 25 mA. The SOA slope efficiency is 0.23 W/A. At the SOA current of 20 mA, the laser slope efficiency would be 0.273 W/A, which translates into 34% differential quantum efficiency of the laser. At higher SOA currents, more than 100% differential quantum efficiency can be achieved this way, i.e., each electron injected into the laser above threshold leads to more than one emitted photon, due to the photon multiplication in the SOA region. The side mode suppression ratio is only about 20 dB (Fig. 21) and it decreases with higher amplifier current (Fig. 25).

Section name	Length [ $\mu\text{m}$ ]	$\kappa$ [1/cm]	DBR Sampled Grating
Left mirror	552	250	12 x 6 $\mu\text{m}$ grating bursts with 46 $\mu\text{m}$ period
Phase tuning	75	-	-
Active	500	-	-
Gain lever	100	-	-
Right mirror	307.5	250	5 x 4 $\mu\text{m}$ grating bursts with 61.5 $\mu\text{m}$ period
Amplifier	500	-	-

Tab. 2 Longitudinal sections of the integrated transmitter ( $\kappa$  – optical coupling coefficient).

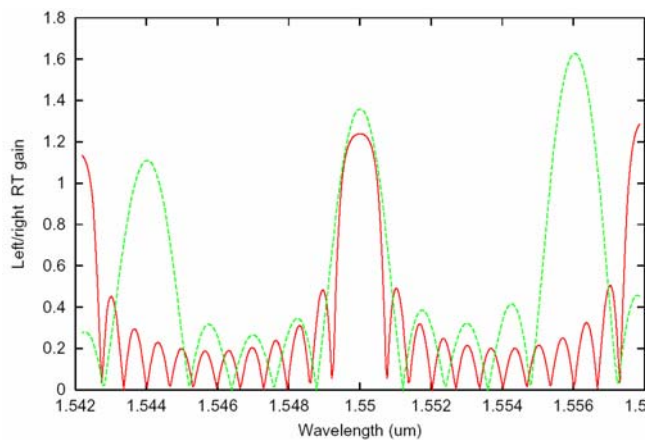


Fig. 20: Round trip gain spectra for left mirror (dashed) and right mirror (solid).

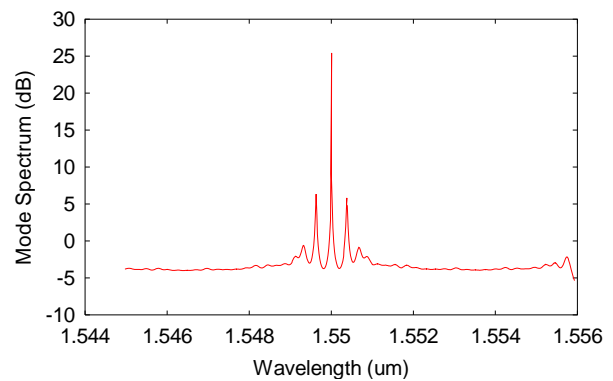


Fig. 21: Calculated mode spectrum (laser current = 25 mA, SOA current = 20 mA).



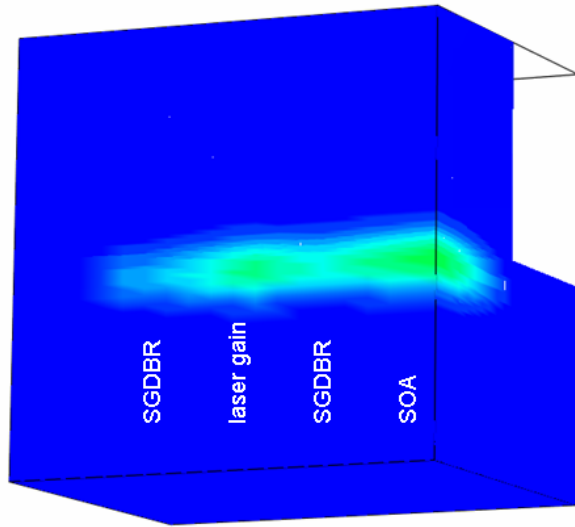


Fig. 22: 3D visualization of the internal light intensity for half the device (laser current = 25 mA, amplifier current = 20 mA).

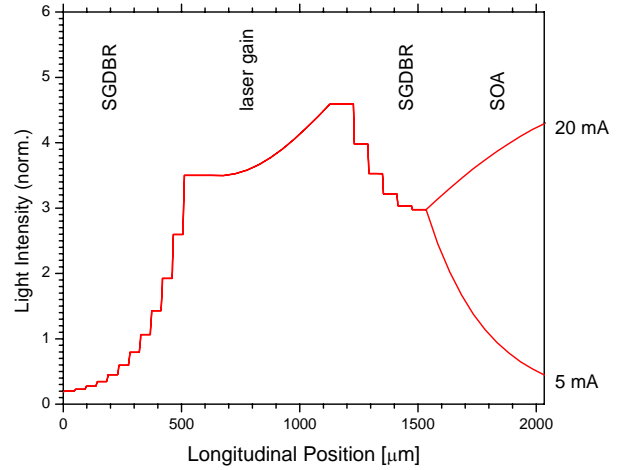


Fig. 23: Longitudinal light intensity profile with 25 mA laser current and with the amplifier current given as parameter.

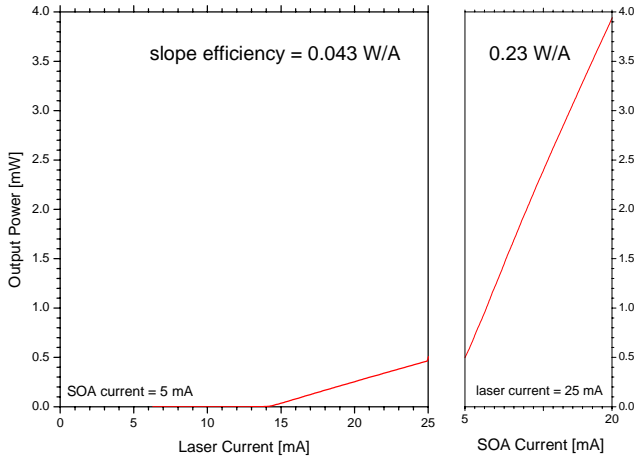


Fig. 24: Calculated light-current characteristics.

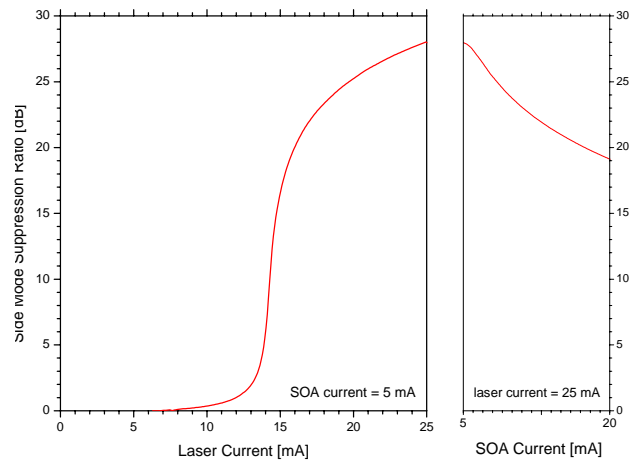


Fig. 25: Calculated side mode suppression ratio vs. current.

#### 4. COMPARISON TO MEASUREMENTS AND PARAMETER CALIBRATION

In this section, we compare our results to the first available receiver measurements in order to validate the model and to calibrate critical material parameters. First, X-ray and photoluminescence (PL) measurements are utilized to adjust MQW parameters. Slight variations from the intended numbers (Tab. 1) are unavoidable during the growth process. For both the quantum wells and the barriers, we extract a slightly lower Ga mole fraction of 0.2367. In addition, the width of both layers is smaller than intended (well: 56.8 Å, barriers: 70.4 Å). Quantum well band-gap renormalization (BGR) is taken into account in order to find agreement with the measured PL peak wavelength (Fig. 26). BGR leads to

decreasing band gap energy with higher carrier density (spectral shift to longer wavelength). The formula used to express BGR is

$$\Delta E_g = A_x \left( \frac{n+p}{2} \right)^{1/3} \quad (3)$$

with  $A_x = 0.8 \times 10^{-10}$  eV/m. The difference to the PL measurement at high energies (low wavelengths) is attributed to the fact that the common free carrier model is currently considered in our gain calculation. Many-body models are expected to correctly reproduce the entire gain spectrum.

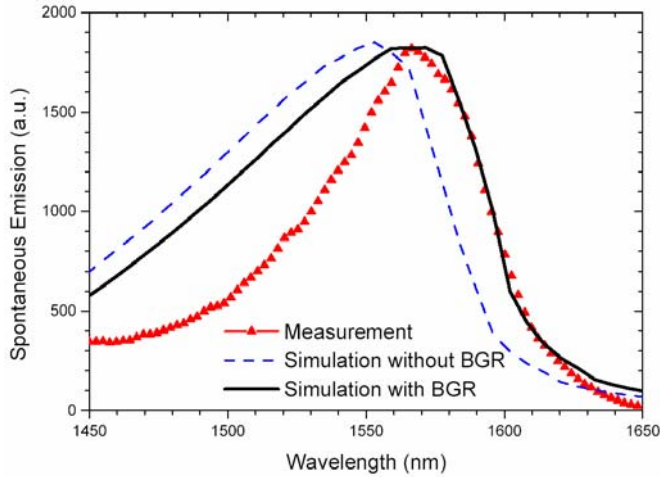


Fig. 26: Comparison between MQW photoluminescence measurement (triangles) and calculated spontaneous emission spectra with and without band-gap renormalization (BGR).

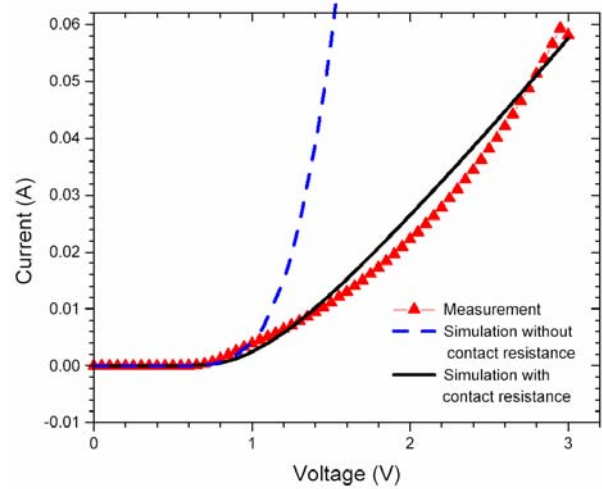


Fig. 27: Dark current versus voltage curve for a 300  $\mu\text{m}$  long SOA.

The measurement of the dark current of a 300  $\mu\text{m}$  long SOA is shown and compared to our simulation in Figure 27. This curve depends on the mobility of the carriers. The mobility depends on the composition of the layer and the doping. Since exact numbers for doping and mobility are unknown, we use  $2200 \text{ cm}^2/\text{Vs}$  for the electron mobility and  $70 \text{ cm}^2/\text{Vs}$  for the hole mobility in all layers. The resulting current-voltage (IV) curve is much steeper than measured (dashed line in Fig. 27). The inclusion of an additional contact resistance of  $52 \Omega$  in the simulation gives a much better agreement with the measurement (solid line in Fig. 27). Future measurements of the contact resistance will allow us to adjust the mobility values.

The contact resistance is known to vary from device to device. IV curves for a 500  $\mu\text{m}$  long SOA are shown in Fig. 28 for different input light power. Here, a contact resistance of  $8.5 \Omega$  is extracted from the fit. Another crucial input parameter is the optical coupling factor between fiber and SOA. Best agreement with the measurements in Fig. 28 is obtained when a coupling factor of 0.163 is assumed for this measurement. With ideal fiber adjustment, a maximum coupling factor of 0.25 is estimated. Thus, less than one quarter of the light power is coupled into our receiver waveguide.

Finally, Fig. 29 compares the calculated receiver photocurrent to the measurement. In this measurement, the ideal fiber coupling factor of 0.25 was achieved. In order to fit the measurement, gain and absorption need to be scaled down by a factor of 0.5 (dip\_factor). This indicates significant inaccuracies of the free carrier model used for gain and absorption calculation. A more accurate model will be applied in future simulations.

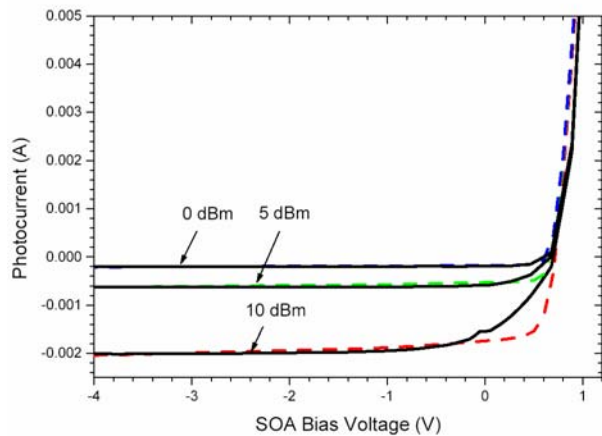


Fig. 28: Photocurrent versus applied reverse voltage for a 500  $\mu\text{m}$  long SOA at different light power in the fiber (dashed: measurement, solid – simulation).

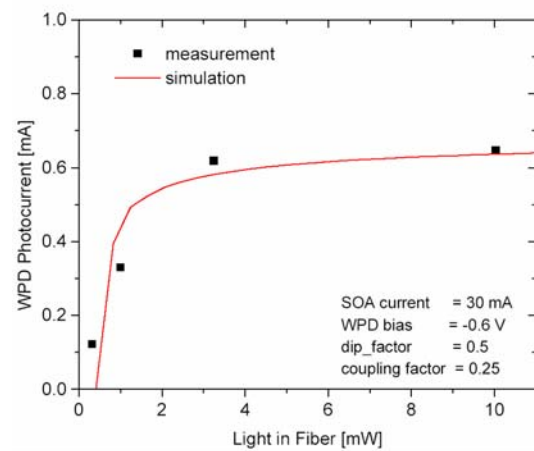


Fig.29: Receiver photocurrent vs. fiber input power.

## 5. SUMMARY

We have presented first results on the self-consistent numerical simulation of an InP-based integrated wavelength converter that monolithically combines optical amplifier, waveguide photodetector, and sampled-grating DBR laser diode. Comparison to available measurements reveals crucial parameters such as the contact resistance and the fiber coupling efficiency. The free carrier model used for quantum well gain and absorption calculations is found to be not accurate enough to achieve agreement with measurements and to predict the device performance. More advanced models will be employed in future simulations.

## ACKNOWLEDGEMENT

This research project is sponsored by the Semiconductor Research Corporation (Award 2001-NJ-968) and by Intel.

## REFERENCES

1. B. Mason, J. Barton, G. A. Fish, L. A. Coldren, S. P. Denbaars, "Design of sampled grating DBR lasers with integrated semiconductor optical amplifiers," *IEEE Phot. Techn. Lett.*, vol. 12, pp. 762-764 (2000).
2. PICS3D by Crosslight Software, 2003.
3. J. Piprek, *Semiconductor Optoelectronic Devices – Introduction to Physics and Simulation*, Academic Press, San Diego, 2003.
4. V. Jayaraman, A. Mathur, L. A. Coldren, and P. D. Dapkus, "Theory, design, and performance of extended tuning range in sampled grating DBR lasers," *IEEE J. Quantum Electron.*, vol. 29, pp. 1824–1834, 1993.